Point mutagenesis in mouse reveals contrasting pathogenetic effects between MEN2B-and Hirschsprung disease-associated missense mutations of the RET gene

Nakatani, Taichi ; Iwasaki, Mitsuhiro ; Yamamichi, Atsuhiro ; Yoshioka, Yuta ; Uesaka, Toshihiro ; Bitoh, Yuko ; Maeda, Kosaku ; Fukumoto,…

(Citation)
Development Growth & Differentiation,62(4):214-222

(Issue Date)
2020-05

(Resource Type)
journal article

(Version)
Accepted Manuscript

(URL)
https://hdl.handle.net/20.500.14094/90007162

Point mutagenesis in mouse reveals contrasting pathogenetic effects between MEN2B- and Hirschsprung disease-associated missense mutations of the RET gene

Taichi Nakatani[1, 2], Mitsuhiro Iwasaki[1], Atsuhiro Yamamichi[1], Yuta Yoshioka[1], Toshihiro Uesaka[1], Yuko Bitoh[2], Kosaku Maeda[3], Takumi Fukumoto[4], Tatsuya Takemoto[5] and Hideki Enomoto[1]

1 Division for Neural Differentiation and Regeneration, Department of Physiology and Cell Biology, Kobe University Graduate School of Medicine, Kobe, Hyogo, Japan

2 Division of Pediatric Surgery, Department of Surgery, Kobe University Graduate School of Medicine, Kobe, Hyogo, Japan

3 Department of Surgery, Hyogo Prefectural Kobe Children's Hospital, Kobe, Hyogo, Japan

4 Division of Hepato-Biliary-Pancreatic surgery, Department of Physiology and Cell Biology, Kobe University Graduate School of Medicine, Kobe, Hyogo, Japan

5 Institute of Advanced Medical Sciences, Tokushima University, Tokushima, Japan

Correspondence: Hideki Enomoto

Division for Neural Differentiation and Regeneration, Department of Physiology and Cell Biology, Kobe University Graduate School of Medicine

7-5-1 Kusunoki-cho, Chuo-ku, Kobe, Hyogo 650-0017, Japan.

Email: enomotoh@med.kobe-u.ac.jp

Abstract

Missense mutations of the *RET* gene have been identified in both multiple endocrine neoplasia (MEN) type 2A/B and Hirschsprung disease (HSCR: congenital absence of the enteric nervous system, ENS). Current consensus holds that MEN2A/B and HSCR are respectively caused by activating and inactivating *RET* mutations. However, the biological significance of *RE*T missense mutations in vivo has not been fully elucidated. In the present study, we introduced one MEN2B-associated (M918T) and two HSCR-associated (N394K and Y791F) *RET* missense mutations into the corresponding regions of the mouse *Ret* gene by genome editing (Ret^{M919T}, Ret^{N396K} and Ret^{Y792F}) and performed histological examinations of *Ret*-expressing tissues to understand the pathogenetic impact of each mutant in vivo. $Ret^{M919T/+}$ mice displayed MEN2B-related phenotypes, including C cell hyperplasia and abnormal enlargement of the primary sympathetic ganglia. Similar sympathetic phenotype was observed in $Ret^{M919T/-}$ mice, demonstrating a strong pathogenetic effect of the *Ret* M919T by a single allele expression. In contrast, no abnormality was found in the ENS of mice harboring the *Ret* N394K or Y791F mutation. Most surprisingly, single allele expression of *RET* N394K or Y791F was sufficient for normal ENS development, indicating that these *RET* mutants exert largely physiological function in vivo. This study reveals contrasting pathogenetic effects between MEN2B- and HSCR-associated *RET* missense mutations, and suggests that some of HSCR-associated *RET*

missense mutations are by themselves neither inactivating nor pathogenetic and require involvement of other gene mutations for disease expressivity.

KEYWORDS

Hirschsprung disease, multiple endocrine neoplasia, RET, gene mutation, genome editing

1 INTRODUCTION

RET is a receptor tyrosine kinase that functions as a signaling receptor for the glial cell line-derived neurotrophic factor (GDNF) family ligands (GFLs). Disruption of the *Ret* gene in mice revealed that RET is essential for development of the enteric, autonomic, and sensory nervous systems and the kidney (Pachnis, Mankoo, & Costantini, 1993). In human, a number of *RET* mutations have been identified in multiple endocrine neoplasia (MEN) type 2A/B and Hirschsprung disease (HSCR) (Wells, Pacini, Robinson, & Santoro, 2013; Tomuschat & Puri, 2015). MEN2A/B patients display medullary thyroid carcinoma (MTC) and pheochromocytoma, which results from the abnormal growth and/or differentiation of thyroid C cells and sympatho-adrenal cells, respectively (Wells et al., 2013). HSCR is characterized by the absence of neural crest-derived enteric ganglia in distal gut. Genetic studies have identified distinct types of *RET* mutations in MEN2A/B and HSCR patients. In MEN2A/B, *RET* mutations affect restricted amino acid residues (one of the cysteine residues in the cysteine-rich domain for MEN2A, and methionine or alanine near the kinase domain for MEN2B). Biochemical analyses of those *RET* mutants revealed higher phosphorylation levels and transforming activity than wild type *RET* (Salvatore et al., 2001; Iervolino et al., 2006). In HSCR, *RET* missense mutations are widely distributed in the *RET* genome; there is no known HSCR-associated 'hot spot' in the *RET* gene. Biochemical analyses of a few HSCR-associated *RET* mutants revealed that they are

functionally impaired. Current consensus holds that MEN2A/B and HSCR are caused by activating and inactivating *RET* mutations, respectively (Krampitz & Norton, 2014). However, many *RET* missense mutations, especially those associated with HSCR, remain uncharacterized, and their biological significance is unclear.

Among HSCR-associated missense mutations, the pathogenetic potential of *RET* N394K and *RET* Y791F remained controversial. N394 is a highly conserved N-linked glycosylation site in RET protein (Bolk et al, 2000), and biochemical studies suggested that N394K mutation alters protein folding and impair cell surface expression of RET (Iwashita, Murakami, Asai, & Takahashi, 1996; Carlomagno et al., 1996). However, another study described that RET N394K is expressed normally on the cell surface and fully functional (Kjær, & Ibáñez, 2003), casting doubt on the pathogenetic effect of this mutation. *RET* Y791F was identified first in HSCR patients (Seri et al., 1997) and later in MTC patients as well (Berndt et al, 1998). However, the most recent large-scale genetic study revealed that there is no association of *RET* Y791F with MTC susceptibility (Toledo et al., 2015). Nonetheless, the potential involvement of *RET* Y791F in HSCR susceptibility has not been discarded. RET Y791F displays ligand-independent monomeric phosphorylation and successive abnormal activation of downstream signaling pathway involving STAT3 (Plaza et al., 2005). Moreover, unlike WT RET, Y791F does not display cell migration-promoting activity when expressed in

HEK293 cells (Hyndman, Gujral, Krieger, Cockburn, & Mulligan, 2013). Because the development of the ENS is exquisitely controlled by RET signaling (Burzynski, Shepherd, & Enomoto, 2009) , these altered biological characteristics could affect ENS development. Overall, it is difficult to characterize the biological significance of *RET* missense mutations using only in vitro approaches.

To understand the impact of *RET* missense mutations on organogenesis, we introduced one MEN2B-associated *RET* mutation (M918T), which has been found in 95% of MEN2B patients, and two HSCR-associated *RET* mutations (N394K and Y791F) into the mouse *Ret* locus by CRISPR/Cas9-mediated genome editing.

2 MATERIAL AND METHODS

2.1 Animals

We used ICR, C57BL/6N, Ret^{EGFP} (Jain et al., 2006), and Ret^{tlz} (Gould, Yonemura, Oppenheim, Ohmori, & Enomoto, 2008) mice in this study. Mice were bred and maintained at the Institute of Experimental Animal Research of Kobe University Graduate School of Medicine under specific pathogen-free conditions. All animal experiments were in compliance with Kobe University Animal Experimentation Regulations.

2.2 Generation of guide RNAs

To design the gRNAs, we used software tool (CC Top https://crispr.cos.uni-heidelberg.de/) to predict unique target sites throughout the mouse genome. To prepare *in vitro*-transcribed gRNAs, a pair of oligos targeting a gene synthesized by Eurofins Genomics was annealed and inserted into the BsaI site of plasmid vectors, which contain a tracrRNA sequence in the downstream of T7 promoter sequence. The sequences of the oligos were as follows: *Ret (*N396K*)* (5′-GCAGTACAGACACGTTGAAATGG-3′), *Ret (*Y792F*)* (5′-ACATGTCATCAAGTTGTATGGGG-3′) and *Ret (*M919T*)* (5′-CCGGATTCCCGTCAAGTGGATGG-3′). After digestion with BsaI, gRNAs were synthesized using the MEGA shortscript T7 Transcription Kit (Thermo Fisher Scientific, Waltham, MA). The synthesized gRNAs were purified by phenol-chloroform extraction and isopropanol precipitation. The precipitated RNA was dissolved in Opti-MEMI (Thermo Fisher Scientific, Waltham, MA) at 2–4 μg/μl, and stored at –80°C until use. The RNAs were quantified by absorption spectroscopy and agarose gel electrophoresis. We used Recombinant Cas9 protein (Alt-R® S.p. HiFi Cas9 Nuclease V3) (Integrated DNA Technologies, Coralville, IA).

2.3 IVF and embryo transfer

Female C57BL/6N mice at postnatal day 26-30 (P26-30) were superovulated by injection with 100 μl of CARD HyperOva® (Kyudo Company, Saga, Japan) 64 hr before in vitro fertilization (IVF) and injection with 200 μl human chorionic gonadotropin 16 hr before IVF. Sperm was collected from the cauda epididymides of mature male C57BL/6 mice (more than P90) and incubated in HTF at 37°C in a humidified incubator containing 5% CO_2 for 1 hr. Ova were collected from the ampulla of the oviduct, and mixed with the sperm in HTF. We obtained ~80 fertilized eggs per a female mouse. After the fertilized eggs were incubated at 37°C in a humidified incubator containing 5% CO_2 for 4 hr, the fertilized eggs were washed with mWM medium (109 mM NaCl, 4 mM KCl, 1 mM KH_2PO_4, 2 mM $MgSO_47H_2O$, 22 mM $NaHCO_3$, 5 mM D-Glucose, 0.2 mM Na-Pyruvate, 2 mM Ca-lactate, 0.2 mM Penicillin G, 0.008 mM Streptomycin, 0.001 mM phenol red, 0.01 mM 2-mercaptoethanol, 0.05 mM EDTA-2Na, 0.004 mM BSA) three times to remove from the sperm. The collected eggs cultured in mWM medium were washed with Opti-MEM I three times to remove the serum-containing medium.

Pseudo pregnant females ICR mice provided by the SLC were prepared for transfer. We were able to obtain ~60 two-cell stage embryos per ~80 fertilized eggs. Approximately 12 hr after electroporation, the two-cell stage embryos were transferred to the oviducts of a recipient ICR. Approximately 10 embryos were transferred to each oviduct, resulting in the

transfer of ~20 embryos per mouse.

2.4 Mutagenesis using CRISPR/Cas9 electroporation of IVF embryos

A pair of custom-made platinum block electrodes (length: 10 mm, width: 3 mm, height: 0.5 mm, gap: 1 mm; BEX, Tokyo, Japan) was used. The electrodes, connected to CUY21 Vivo-SQ (BEX, Tokyo, Japan), were set under a stereoscopic microscope. 60 eggs prepared by IVF were subjected to electroporation at one time. The eggs were placed in a line in the electrode gap filled with Opti-MEM I solution containing gRNA and Cas9 protein and single-stranded oligo DNA nucleotides (ssODNs; total 5 μl volume), and electroporation was performed. The ssODNs synthesized by Eurofins Genomics (Luxembourg, Luxembourg) were dissolved in Opti-MEMI to 4 μg/μl, and stored at –20°C until use. 400 ng/μl ssODNs were introduced together with 200 ng/μl Cas9 mRNA and 100 ng/μl gRNA. The sequences of the ssODNs were as follows: *Ret* (N396K) (5′-CTGGTCAACGACTCAGACTTCCAGGGGCCTGGGGCAGGTGGGATCCTCGTCCTC CATTTCAAGGTGTCTGTACTGCCCGTCACCCTGAACCTACCCAGGGCCTACTCCTTC CCAGTGAAT-3′), *Ret* (Y792F) (5′-TACGAGACCTGCTGTCTGAATTCAACCTTCTGAAACAAGTCAACCATCCACATG TCATCAAGTTGTTTGGCGCCTGCAGCCAGGATGGTAAGGCTAACCAGATGATAGGG

TGGGCGGGCGGGTGGGCAGCTGC-3′) and *Ret* (M919T) (5′-GAGCCATACTAATGCCTTCGTTCACTACCTCTAGGGCCGGATCCCCGTCAAGTG GACCGCAATTGAGTCCCTTTTCGATCACATCTATACTACTCAAAGTGATGTGTAAGT GA-3′). Each ssODN was designed such that it introduces an expected disease-associated mutation and two silent mutations that generate a new restriction enzyme recognition site and a mutated protospacer adjacent motif (PAM) sequence.

The electroporation conditions were 25 V (3 msec ON + 97 msec OFF) × 5 times. After electroporation, the eggs were immediately collected from the electrode chamber and subjected to three washes with mWM medium. The eggs were cultured overnight in mWM medium in a humidified incubator containing 5% CO_2.

2.5 Genotyping analysis

Primer sequences for genotyping of mutation mice were as follows: *Ret* (N396K) forward (5′-GAGTCCTGCAGCTCGCGGTCC-3′), reverse (5′-CCATGTAATGGGCCACGGGCT-3′), *Ret* (Y792F) forward (5′-CTGGATGCTGAGGGTCTCCGTGTA-3′), reverse (5′-GCCCACCCTATCATCTGGTTAGCC-3′) and *Ret* (M919T) forward (5′-GCACAGTTGGTCTGTCCCTGGGACA-3′) and reverse

(5′-GCAACGGCCTCACTTACACATCACT-3′) primers. The sizes of PCR products generated from *Ret* (N396K), *Ret* (Y792F), and *Ret* (M919T) were 188, 260, and 433 bp, respectively. Each amplified product was the same sizes as wild type. Mutant amplified genes were digested by EcoRI or BamHI. Mutant bands for *Ret* (N396K), *Ret* (Y792F), and *Ret* (M919T) displayed 125/63, 165/95, and 344/89 bp, respectively. PCR products showing restriction fragment DNA patterns were subjected to sequence analysis.

2.6 Histological analysis

Methods for whole-mount 5-bromo-4-chloro-3-indolyl-β-D-galactopy-ranoside (X-gal) staining, whole-mount acetylcholinesterase (AChE) staining, dihydronicotinamide adenine dinucleotide phosphate diaphorase (NADPH-d) staining, immunohistochemistry experiments are described elsewhere (Enomoto et al., 1998; Enomoto et al., 2004; Uesaka, Nagashimada, & Enomoto, 2013). The primary antibodies used for immunohistochemistry were rabbit anti-GFP (green fluorescent protein; 1:1000; Aves Labs, Tigard, OR), and sheep anti-TH (tyrosine hydroxylase; 1:500; Merck Millipore, Burlington, MA). To detect GFP signals, secondary antibodies conjugated with Alexa Fluor 488 donkey anti rabbit IgG (1:500; Thermo Fisher Scientific, Waltham, MA). To detect TH signals, biotin-SP-conjugated donkey anti-sheep (1:200; Jackson ImmunoResearch, West Grove, PA) and peroxidase conjugated with

streptavidin (1:200; Jackson ImmunoResearch, West Grove, PA).

Fluorescent imaging was performed using a Zeiss Axioskop 2FS plus system (Zeiss, Oberkochen, Germany). Confocal images were acquired using a LSM5 PASCAL system (Zeiss, Oberkochen, Germany). Representative images were selected from animals or experiments that had been repeated at least three times

2.7 In situ hybridization

In situ hybridization (ISH) was performed as described previously (Enomoto et al., 2004). All riboprobes for ISH were synthesized using the DIG RNA Labeling Kit (Roche Diagnostics, Mannheim, Germany) as specified by the manufacturer. Digoxigenin (DIG) - labeled cRNA probes were generated using a DNA fragment encompassing bases 402–848 of the *Calcitonin* cDNA (adenine of the initiator Met is assigned as 1) as template. The hybridized DIG-labeled probes were detected by anti-DIG antibody conjugated with alkaline phosphatase (1:2000, Roche Diagnostics, Mannheim, Germany) and exposure with NBT (nitroblue tetrazolium) / BCIP (5-bromo-4-chloro-3-indolyl phosphate, toluinium salt) color substrates (Rosche Diagnostics, Mannheim, Germany).

2.8 Quantitative analysis

Quantitative analysis of cell number in the myenteric plexus was performed after staining with NADPH-d staining. Numbers of enteric neurons per area were manually counted in a blinded fashion. Twenty regions were randomly selected from the 200× fields of the myenteric plexus of the small intestine and colon in P8 mice. Myenteric fiber counts were performed on acetylcholinesterase-stained myenteric plexus of the small intestine at P8 by counting fibers crossing a grid (Gianino, Grider, Cresswell, Enomoto, & Heuckeroth, 2003) with eight horizontal and eight vertical lines.

2.9 Statistical analysis

Statistical analyses were performed in GraphPad Prism software (version 5, Software Inc.) and data are presented as means ± SEM. Comparison between individual groups was performed by Mann–Whitney U test.

3 Results

3.1 Generation of mice harboring *Ret* missense mutations by genome editing

To assess the biological significance of MEN2B- and HSCR-associated *RET* mutations, we chose three *RET* missense mutations, M918T, N394K and Y791F (Figure 1a).

RET M918T is the most common mutation found in MEN2B. *RET* N394K and Y791F have been identified in HSCR and expected to impair N-linked glycosylation and ligand-dependent activation of RET protein, respectively (Kjær & Ibáñez, 2003; Sawai et al., 2005). We introduced these mutations into the corresponding regions of the mouse *Ret* genome (N396, Y792 and M919) by electroporation-mediated genome editing (Hashimoto & Takemoto, 2015) (for details, see Material and Methods). In brief, for each mutagenesis, we electroporated gRNA, Cas9 and ssODN into mouse zygotes. gRNA was designed to cleave the *Ret* genome near the mutation site, whereas ssODN was designed to introduce the expected mutations (N396K, Y792F and M919T), and multiple silent mutations to disrupt PAM sequence and to generate a new restriction enzyme recognition site for genotyping (Figure 1b-d, left). Founder mice harboring the expected mutations were crossed to wild type mice (C57BL/6N) to obtain F1 mice, which were maintained (Figure 1b-d, genotyping is shown on right) and subjected to histological analyses.

3.2 Mice carrying *Ret* M919T mutation display MEN2B-related phenotypes

MEN2B patients display MTC and pheochromocytoma, which derive from thyroid C cells and sympatho-adrenal cells, respectively. We performed in situ hybridization analysis of the thyroid gland using riboprobes detecting *calcitonin*, a C-cell specific marker. Although C

cells were distributed relatively evenly around the thyroid follicles in wild type (WT) mice, they were often aggregated and showed nodular expansion, which disrupted the follicular structure, in $Ret^{M919T/+}$ mice (6 months, Figure 2a). This result indicates that *Ret* M919T mutation induces C cell hyperplasia, a precancerous lesion leading to MTC.

To understand how *Ret* M919T mutation affects the development of *Ret*-expressing tissues globally, we crossed $Ret^{M919T/+}$ mice to $Ret^{tlz/+}$ mice and obtained $Ret^{M919T/tlz}$ and $Ret^{+/tlz}$ mice. The *Ret–tlz* allele is *Ret*-null and expresses *tauLacZ* (*tlz*) gene encoding tau-β-galactosidase under the *Ret* promoter, which enables visualization of *Ret*-expressing tissues by X-gal staining (Gould et al., 2008). We found that the primary sympathetic chain is abnormally enlarged in $Ret^{M919T/tlz}$ embryos at embryonic day 11.5 (E11.5, $n = 5$) as compared to the control (Figure 2b, arrows, $n = 5$). This was further confirmed by whole-mount TH staining of E13.5 embryos (Figure 2e, arrows, $n = 6$). Thus, single-allele expression of *Ret* M919T is sufficient to cause the abnormal enlargement of the sympathetic ganglia. Other *Ret*-expressing tissues including the trigeminal and dorsal root ganglia, and kidneys appeared normal in $Ret^{M919T/tlz}$ embryos by X-gal staining (arrows in Figure 2c, d). The ENS also developed normally in $Ret^{M919T/tlz}$ mice (Figure 3, 4, see below). These results demonstrate that *Ret* M919T mutation is strongly pathogenetic and specifically affects the development and/or differentiation of thyroid C cells and sympatho-adrenal cells in mice.

3.3 ENS develops normally in mice harboring *Ret* N396K or Y792F mutation

We next examined whether *Ret* N396K or Y792F exerts an adverse effect on the ENS development. Mice carrying *Ret* N396K or Y792F mutation in a heterozygous manner ($Ret^{N396K/+}$ or $Ret^{Y792F/+}$ mice) lived up to adult with no apparent abnormality (data not shown). Thus, we challenged these mice by genetic crossing. Previous genetic studies demonstrated that reduced levels of *RET* expression confers susceptibility to HSCR (Burzynski et al, 2009). In mice, the development of the ENS is impaired when *Ret* expression is decreased to slightly less than half of its normal level (Uesaka, Nagashimada, Yonemura, & Enomoto, 2008). Therefore, single allele-only expression of the mutant allele allows the most stringent assessment of the pathogenetic effect, if any, of the *Ret* mutant allele. To this end, we crossed $Ret^{N396K/+}$ and $Ret^{Y792F/+}$ mice to $Ret^{EGFP/+}$ or $Ret^{tlz/+}$ mice to generate $Ret^{N396K/EGFP}$, $Ret^{Y792F/EGFP}$, $Ret^{N396K/tlz}$ and $Ret^{Y792F/tlz}$ mice in which only the mutant *Ret* is expressed in a mono-allelic fashion. The *Ret-EGFP* allele is *Ret*-null and expresses EGFP under the *Ret* promoter, which allows visualization of ENS precursors by their EGFP fluorescence (Jain et al., 2006). Surprisingly, examination of the ENS by both EGFP fluorescence (E12.5) and X-gal staining (E15.5) revealed no abnormality in ENS development in these embryos (Figure 3a, b; $Ret^{+/EGFP}$, $n = 6$; $Ret^{N396K/EGFP}$, $n = 3$; $Ret^{Y792F/EGFP}$, $n = 5$; $Ret^{M919T/EGFP}$, $n = 5$; $Ret^{+/tlz}$, $n = 6$; $Ret^{N396K/tlz}$, $n = 6$;

Ret $^{Y792F/tlz}$, n = 7; *Ret* $^{M919T/tlz}$, n = 3), indicating that migration of ENS precursors is unaffected by *Ret* N396K or Y792F mutation.

To assess the structure of the ENS in more detail, we performed NADPH-d staining and acetylcholine esterase (AChE) histochemistry of the gut (P8), which visualize inhibitory motor and the other enteric neurons, respectively. In both forms of staining, the ENS structure and neuron density appeared comparable between WT, $Ret^{N396K/tlz}$ and $Ret^{Y792F/tlz}$ mice (Figure 4a, c, twenty randomly selected fields from each mouse evaluated). Moreover, we found no significant difference in the numbers of NADPH-d positive neurons among these animals (Figure 4b, small intestine: WT 84.5±9.7, n = 3; $Ret^{N396K/tlz}$ 83.2±15.7, n = 3; $Ret^{Y792F/tlz}$ 84.1±5.1, n = 3; WT vs $Ret^{N396K/tlz}$, p=0.5516; WT vs $Ret^{Y792F/tlz}$, p=0.4274: colon WT 461±13.6, n = 3; $Ret^{N396K/tlz}$ 446.7±15.6, n = 3; $Ret^{Y792F/tlz}$ 451.7±12.9, n = 3; WT vs $Ret^{N396K/tlz}$, p=0.3831; WT vs $Ret^{Y792F/tlz}$, p=0.5203). Although we also attempted to count the numbers of AChE-positive neurons, thick nerve fibers and densely packed neurons hampered reliable counting at this postnatal period (P8). Therefore, we measured the density of AChE-positive nerve fibers, but again observed no difference between WT and mutant ($Ret^{N396K/tlz}$ or $Ret^{Y792F/tlz}$) mice (Figure 4d, WT 79.4±4.1, n = 3; $Ret^{N396K/tlz}$ 82.8±6.5, n = 3; $Ret^{Y792F/tlz}$ 83.0±6.2, n = 3: WT vs $Ret^{N396K/tlz}$, p=0.3957; WT vs $Ret^{Y792F/tlz}$, p=0.3129). These results indicate that *Ret* N396K and Y792F exert no adverse effect in vivo, even when they are expressed in a mono-allelic fashion.

4 DISCUSSION

Although a wide variety of missense mutations are found in human diseases, the biological significance of most of those mutations has been left uninvestigated in vivo. This was mainly due to the technical difficulty of point mutagenesis by gene targeting, which has been widely used to introduce targeted mutations. Recent advances in genome editing have revolutionized targeted mutagenesis in vivo. In particular, electroporation-mediated genome editing in mouse zygotes is one of the most powerful techniques, as it enables generation of mice carrying a point mutation by a single electroporation (Hashimoto & Takemoto, 2015). Using this technology, we investigated pathogenetic potential of HSCR- and MEN2B-associated *RET* missense mutations by introducing them into the corresponding regions of the mouse *Ret* gene. Although MEN2B-related phenotypes were easily recapitulated in mice carrying a MEN2B mutation (*Ret* M919T), no HSCR-related phenotype (impaired development of the ENS) was detected in mice harboring the HSCR-associated mutations, *Ret* N396K and Y792F. This study thus reveals contrasting biological effects between MEN2B- and HSCR-associated mutations in mouse organogenesis.

Mice carrying *Ret* M919T mutation that we generated in this study displayed a

phenotype closely similar to that of the MEN2B-knockin mice previously reported (Smith-Hicks, Sizer, Powers, Tischler, & Costantini, 2000), including C-cell hyperplasia and enlargement of the sympathetic ganglia. However, there are significant differences in these two MEN2B mouse models. First, in MEN2B-knockin mouse line, the sympathetic ganglion phenotype was observed only in mice carrying the mutation in a homozygous manner (referred to as $Ret^{M919TKi/M919T\ Ki}$). Second, mice carrying M919TKi and kinase-dead *Ret* null allele ($Ret^{M919TKi/Ret\ K-}$) did not show any abnormal phenotypes (Smith-Hicks et al., 2000). Importantly, the M919T allele that we generated in the present study exerted the abnormal sympathetic ganglion phenotype even on mono-allelic expression (Figure 2), and this result revises the dosage-dependent pathogenetic effect by RET M919T implied in the previous study. The exact cause of this discrepancy is unclear. However, the *Ret* M919T Ki allele was generated by gene targeting and harbored 70 bp sequence (loxP and polylinkers) inserted into an intron region of the *Ret* gene. Although RT-PCR assay of the brain tissue showed that *Ret* M919T Ki allele was properly expressed (Smith-Hicks et al., 2000), it is still possible that this aberrant insertion affects *Ret* expression in a tissue-specific fashion. The *Ret* M919T allele used in our study has a minimal modification in the *Ret* genome and exerts a strong pathogenetic effect of the *Ret* M919T mutation by mono-allelic expression. Our study demonstrates the power of genome editing technology in investigating the biological significance of point mutations identified in

human diseases.

Previous studies on human RET N394K and Y791F (corresponding to mouse RET N396K and Y792F) revealed conflicting results with regard to their potential pathogenicity. This could be caused by different sensitivities or specificities associated with in vitro assays, and in vivo examination was necessary. To our surprise, no abnormality was detected in the ENS of $Ret^{N396K/-}$ and $Ret^{Y792F/-}$ mice, indicating that single-allele only expression of the mutant allele is sufficient for normal development of the ENS. Moreover, we found no abnormality in other Ret-expressing tissues, including the sensory, motor and autonomic ganglia, and the kidney of $Ret^{N396K/tlz}$ and $Ret^{Y792F/tlz}$ mice (revealed by X-gal staining of E12.5 embryos, data not shown), suggesting that RET N394K and Y791F are almost fully functional RET proteins. This study provides a conclusive resolution to controversies about these mutations: *Ret* N396K or Y792F mutation per se exerts no pathogenetic effect in vivo at least in mice. This evidence presents a cautionary counter-example to the general notion that HSCR-associate RET mutations are inactivating mutations. Genetic studies of familial HSCR revealed complex inheritance pattern, and isolated HSCR is considered to be a multifactorial disease involving multiple gene mutations [29]. Given a wide variety of *RET* missense mutations identified in HSCR, some of those mutations can be minimally pathogenetic and requires mutations of other genes for the disease expressivity. Future studies will be required to address this question.

In HSCR patients, many different types of missense mutations of the *RET* gene have been identified, and they are widely distributed in the *RET* genome. Among those, *RET* C620R was previously characterized in vivo, which showed that C620R mutation impairs RET function due to loss of cell surface expression of the mutant RET protein (Carniti et al, 2006). However, this mutation is special in that it was found in patients displaying both MEN2A and HSCR. In other words, mutations found only in HSCR patients have largely left uncharacterized in vivo. The results reported here clearly demonstrate that some of HSCR-associated *RET* missense mutations are neither inactivating nor pathogenetic. Other types of *RET* missense mutations should be further investigated by in vivo mutagenesis to deepen our understanding of the pathogenetic mechanisms of HSCR.

Acknowledgements

The authors thank Y. Takase for excellent technical assistances. They also thank D. Sipp for editing this manuscript. This work was supported by Japan Society for the Promotion of Science (JSPS), KAKENHI, Grant/Award Number: 17H03550, 17K19527, and Yakult Bio-Science Foundation

Reference

Berndt, I., Reuter, M., Saller, B., Frank-Raue, K., Groth, P., Grussendorf, M., … Höppner, W. (1998). A new hot spot for mutations in the ret protooncogene causing familial medullary thyroid carcinoma and multiple endocrine neoplasia type 2A. The Journal of Clinical Endocrinology and Metabolism, 83, 770-774. https://doi.org/10.1210/jcem.83.3.4619

Bolk, S., Pelet, A., Hofstra, RM., Angrist, M., Salomon, R., Croaker, D., … Chakravarti A. (2000). A human model for multigenic inheritance: phenotypic expression in Hirschsprung disease requires both the RET gene and a new 9q31 locus. Proceedings of the National Academy of Sciences of the United States of America , 97, 268-273. https://doi.org/10.1073/pnas.97.1.268

Uesaka T , G., Shepherd, IT., & Enomoto, H. (2009). Genetic model system studies of the development of the enteric nervous system, gut motility and Hirschsprung's disease. Neurogastroenterology & Motility, 21, 113-127. https://doi.org/10.1111/j.1365-2982.2008.01256.x.

Carlomagno, F., De Vita, G., Berlingieri, MT., de Franciscis, V., Melillo, RM., Colantuoni, V., … Santoro, M. (1996). Molecular heterogeneity of RET loss of function in Hirschsprung's disease. The EMBO Journal, 3, 15, 2717-2725. https://doi.org/10.2353/ajpath.2006.050607

Enomoto, H., Araki, T., Jackman, A., Heuckeroth, RO., Snider, WD., Johnson, EM. Jr., &

Milbrandt, J. (1998). GFR alpha1-deficient mice have deficits in the enteric nervous system and kidneys. Neuron, 1998, 21, 317-324. https://doi.org/10.1016/s0896-6273(00)80541-3

Enomoto, H., Hughes, I., Golden, J., Baloh, RH., Yonemura, S., Heuckeroth, RO., … Milbrandt J. (2004). GFRalpha1 expression in cells lacking RET is dispensable for organogenesis and nerve regeneration. Neuron, 18, 44, 623-636. https://doi.org/10.1016/j.neuron.2004.10.032

Carniti, C., Belluco, S., Riccardi, E., Cranston, AN., Mondellini, P., Ponder, BA., … Bongarzone, I. (2006). The Ret(C620R) mutation affects renal and enteric development in a mouse model of Hirschsprung's disease. The American Journal of Pathology, 168, 1262-1275.

Gianino, S., Grider, JR., Cresswell, J., Enomoto, H., & Heuckeroth, RO. (2003). GDNF availability determines enteric neuron number by controlling precursor proliferation. Development, 130, 2187-2198. https://doi.org/10.1242/dev.00433

Gould, TW., Yonemura, S., Oppenheim, RW., Ohmori, S., & Enomoto, H. (2008). The neurotrophic effects of glial cell line-derived neurotrophic factor on spinal motoneurons are restricted to fusimotor subtypes. Journal of Neuroscience, 28, 2131–2146. https://doi.org/10.1523/JNEUROSCI.5185-07.2008

Hashimoto, M. & Takemoto, T. (2015). Electroporation enables the efficient mRNA delivery into the mouse zygotes and facilitates CRISPR/Cas9-based genome editing. Scientific Reports, 11, 11315. https://doi.org/10.1038/srep11315

Hyndman, BD., Gujral, TS., Krieger, JR., Cockburn, JG., & Mulligan, LM. (2013). Multiple functional effects of RET kinase domain sequence variants in Hirschsprung disease. Human Mutation, 34, 132-142. https://doi.org/10.1002/humu.22170

Iervolino, A., Iuliano, R., Trapasso, F., Viglietto, G., Melillo, RM., Carlomagno, F., … Fusco, A. (2006). The receptor-type protein tyrosine phosphatase J antagonizes the biochemical and biological effects of RET-derived oncoproteins. Cancer Research, 15, 66, 6280-6287. https://doi.org/10.1158/0008-5472.CAN-06-0228

Iwashita, T., Murakami, H., Asai, N., & Takahashi, M. (1996). Mechanism of ret dysfunction by Hirschsprung mutations affecting its extracellular domain. Human Molecular Genetics, 5, 1577-1580. https://doi.org/10.1093/hmg/5.10.1577

Jain, S., Golden, JP., Wozniak, D., Pehek, E., Johnson, EM. Jr., & Milbrandt, J. (2006). RET is dispensable for maintenance of midbrain dopaminergic neurons in adult mice. Journal of Neuroscience, 26, 11230-11238. https://doi.org/10.1523/JNEUROSCI.1876-06.2006

Kjær, S., & Ibáñez, CF. (2003). Intrinsic susceptibility to misfolding of a hot-spot for Hirschsprung disease mutations in the ectodomain of RET. Human Molecular Genetics, 12, 2133-2144. https://doi.org/10.1093/hmg/ddg227.

Krampitz, GW., & Norton, JA. (2014). RET gene mutations (genotype and phenotype) of multiple endocrine neoplasia type 2 and familial medullary thyroid carcinoma. Cancer, 120,

1920-1931. https://doi.org/10.1002/cncr.28661

Pachnis, V., Mankoo, B., & Costantini, F. (1993). Expression of the c-ret proto-oncogene during mouse embryogenesis. Development, 119, 1005-1017.

Plaza, Menacho, I., Koster, R., van der, Sloot, AM., Quax, WJ., Osinga, J., van der, Sluis, T., … Hofstra, RM. (2005). RET-familial medullary thyroid carcinoma mutants Y791F and S891A activate a Src/JAK/STAT3 pathway, independent of glial cell line-derived neurotrophic factor. Cancer Research, 65, 1729-1737. https://doi.org/10.1158/0008-5472.CAN-04-2363

Salvatore, D., Melillo, RM., Monaco, C., Visconti, R., Fenzi, G., Vecchio, G., … Santoro M. (2001). Increased in vivo phosphorylation of ret tyrosine 1062 is a potential pathogenetic mechanism of multiple endocrine neoplasia type 2B. Cancer Research, 15, 61, 1426-1431.

Sancandi, M., Ceccherini, I., Costa, M., Fava, M., Chen, B., Wu, Y., …Tam PK. (2000). Incidence of RET mutations in patients with Hirschsprung's disease. Journal of Pediatric Surgery, 35, 139-142. https://doi.org/10.1016/s0022-3468(00)80031-7

Sawai, H., Okada, Y., Kazanjian, K., Kim, J., Hasan, S., Hines OJ., … Eibl G. (2005). The G691S RET polymorphism increases glial cell line-derived neurotrophic factor-induced pancreatic cancer cell invasion by amplifying mitogen-activated protein kinase signaling. Cancer Research, 15, 65, 11536-11544. https://doi.org/10.1158/0008-5472.CAN-05-2843

Seri, M., Yin, L., Barone, V., Bolino, A., Celli, I., Bocciardi, R., … Romeo, G. (1997).

Frequency of RET mutations in long- and short-segment Hirschsprung disease. Human Mutation, 9, 243-249. https://doi.org/10.1002/(SICI)1098-1004(1997)9:3<243::AID-HUMU5>3.0.CO;2-8

Smith-Hicks, CL., Sizer, KC., Powers, JF., Tischler, AS., & Costantini, F. (2000). C-cell hyperplasia, pheochromocytoma and sympathoadrenal malformation in a mouse model of multiple endocrine neoplasia type 2B. The EMBO Journal, 19, 612-622. https://doi.org/10.1093/emboj/19.4.612

Sweetser, DA., Froelick, GJ., Matsumoto, AM., Kafer, KE., Marck, B., Palmiter, RD., & Kapur RP. (1999). Ganglioneuromas and renal anomalies are induced by activated RET(MEN2B) in transgenic mice. Oncogene, 28, 18, 877-886. https://doi.org/10.1038/sj.onc.1202376

Toledo, RA., Hatakana, R., Lourenço, DM, Jr., Lindsey, SC., Camacho, CP., Almeida, M., …Toledo, SP. (2015). Comprehensive assessment of the disputed RET Y791F variant shows no association with medullary thyroid carcinoma susceptibility. Endocrine-Related Cancer, 22, 65-76. https://doi.org/10.1530/ERC-14-0491

Tomuschat, C., & Puri, P. (2015). RET gene is a major risk factor for Hirschsprung's disease: a meta-analysis. Pediatric Surgery International, 31, 701-710. https://doi.org/10.1007/s00383-015-3731-y

Uesaka, T., Nagashimada, M., Yonemura, S., & Enomoto, H. (2008). Diminished Ret

expression compromises neuronal survival in the colon and causes intestinal aganglionosis in mice. Journal of Clinical Investigation, 118, 1890-1898. https://doi.org/10.1172/JCI34425

Uesaka, T., Nagashimada, M., & Enomoto, H. (2013). GDNF signaling levels control migration and neuronal differentiation of enteric ganglion precursors. Journal of Neuroscience, 9, 33, 16372-16382. https://doi.org/10.1523/JNEUROSCI.2079-13.2013

Wells, SA, Jr., Pacini. F., Robinson, BG., & Santoro, M. (2013). Multiple endocrine neoplasia type 2 and familial medullary thyroid carcinoma: an update. The Journal of Clinical Endocrinology and Metabolism, 98, 3149-3164. https://doi.org/10.1210/jc.2013-1204

Figure Legends

FIGURE 1. Generation of mice harboring *Ret* missense mutations by the CRISPR-Cas9 system.

(a) A schematic showing the location of the *RET* missense mutations analyzed in this study. CLD: cadherin-like domain; TM: transmembrane domain. (b-d) (Left) Sequence analyses and PCR genotyping of the *Ret (*N396K*)*, *Ret (*Y792F*)* and *Ret (*M919T*)* alleles. Altered amino acids due to the missense mutation are encircled. Overlines indicate PAM sequences (NGG) and the following nucleotides targeted by the sgRNA. The lane 'ssODN' shows a part of ssODN sequences that include the missense mutation and two silent mutations: one of which disrupting PAM and the other introducing a new restriction enzyme recognition site. Note that, for the *Ret (*M919T*)* allele, introducing the missense mutation simultaneously disrupts PAM sequence. Images of gel electrophoresis show representative genotyping results of WT and heterozygous mutant (Mu) mice. After restriction enzyme digestion of the PCR products, WT vs. mutant bands appear as (188 bp) vs. (125 and 63 bp), (260 bp) vs. (165 and 95bp), and (433 bp) vs. (344 and 89 bp) for the *Ret (*N396K*)*, *Ret (*Y792F*)* and *Ret (*M919T*)* alleles, respectively. The 63 bp mutant band in the gel (b) overlapped primer dimers and could not be distinguished.

FIGURE 2. Mice carrying *Ret* M919T mutation display MEN2B-related phenotypes

(a) In situ hybridization analysis of the thyroid gland of 6 month-old mice using calcitonin riboprobes. Higher magnification picture is shown on right. Note the presence of nodular C cell hyperplasia in $Ret^{M919T/+}$ mice (right). Scale bars: 100 μm and 20 μm for left and right. (B-D) Whole-mount X-gal staining of E11.5 embryos. (b) The sympathetic trunk (white arrows) was abnormally thick in $Ret^{M919T/tlz}$ embryos. Scale bar: 500 μm (c, d) The trigeminal ganglia (white arrowheads), dorsal root ganglia (black arrows) and kidneys (black arrowheads) were comparable between $Ret^{+/tlz}$ and $Ret^{M919T/tlz}$ embryos. Scale bars: 500 μm (e) Whole-mount TH immunohistochemistry of E13.5 embryos showed abnormal enlargement of the primary sympathetic chain (white arrows) in $Ret^{M919T/tlz}$ mice. Scale bar: 500 μm

FIGURE 3. *Ret* missense mutations, N396K, Y792F, *and* M919T, have no impact on the gut colonization by ENS precursors.

(a) Whole-mount EGFP staining of embryonic gut (E12.5). Arrows indicate the location of most advanced ENS precursors. No difference was observed in $Ret^{+/EGFP}$, $Ret^{N396K/EGFP}$, $Ret^{Y792F/EGFP}$ and $Ret^{M919T/EGFP}$ embryos. Scale bar: 250 μm. (b) Whole-mount X-gal staining of the distal colon at E15.5 in $Ret^{+/tlz}$, $Ret^{N396K/tlz}$, $Ret^{Y792F/tlz}$ and $Ret^{M919T/tlz}$. Colonization pattern by ENS precursors were comparable between all genotypes. Scale bar: 250 μm.

FIGURE 4. Quantitative analysis of enteric neurons in mice carrying *Ret* missense mutations

(a) Representative images of NADPH-d staining of the small intestine, showing comparable staining patterns in WT, $Ret^{N396K/tlz}$, $Ret^{Y792F/tlz}$ and $Ret^{M919T/tlz}$ mice (P8). Scale bar: 100 μm. (b) Bar graphs showing the numbers of neurons visualized by NADPH-d-staining in the small intestine (left) and colon (right). Error bars: SEM. (c) The structure of the ENS (small intestine, P8) visualized by AChE staining. Scale bar: 100 μm. (d) Bar graph showing the density of AChE-positive fibers in the myenteric plexus of the small intestine. Error bars: SEM.

FIGURE 1. Generation of mice harboring Ret missense mutations by the CRISPR-Cas9 system. (a) A schematic showing the location of the RET missense mutations analyzed in this study. CLD: cadherin-like domain; TM: transmembrane domain. (b-d) (Left) Sequence analyses and PCR genotyping of the Ret (N396K), Ret (Y792F) and Ret (M919T) alleles. Altered amino acids due to the missense mutation are encircled. Overlines indicate PAM sequences (NGG) and the following nucleotides targeted by the sgRNA. The lane 'ssODN' shows a part of ssODN sequences that include the missense mutation and two silent mutations: one of which disrupting PAM and the other introducing a new restriction enzyme recognition site. Note that, for the Ret (M919T) allele, introducing the missense mutation simultaneously disrupts PAM sequence. Images of gel electrophoresis show representative genotyping results of WT and heterozygous mutant (Mu) mice. After restriction enzyme digestion of the PCR products, WT vs. mutant bands appear as (188 bp) vs. (125 and 63 bp), (260 bp) vs. (165 and 95bp), and (433 bp) vs. (344 and 89 bp) for the Ret (N396K), Ret (Y792F) and Ret (M919T) alleles, respectively. The 63 bp mutant band in the gel (b) overlapped primer dimers and could not be distinguished.

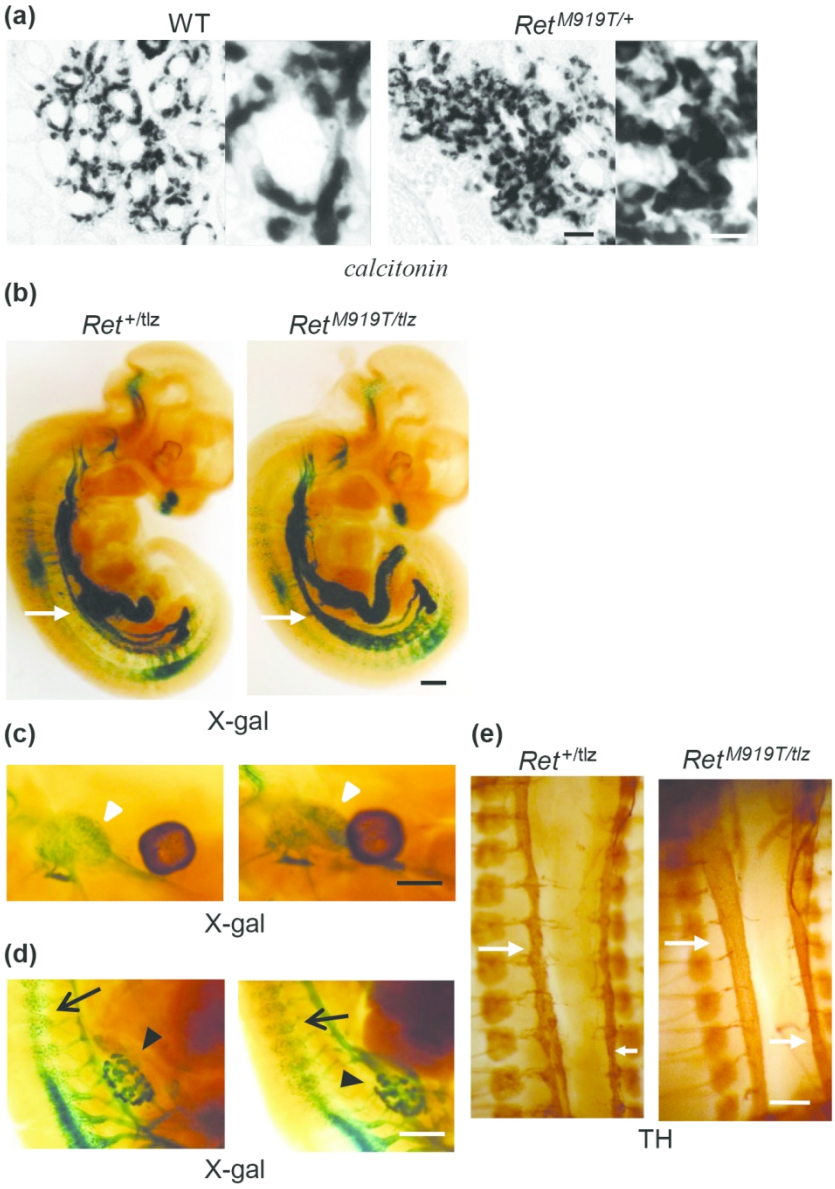

FIGURE 2. Mice carrying Ret M919T mutation display MEN2B-related phenotypes
(a) In situ hybridization analysis of the thyroid gland of 6 month-old mice using calcitonin riboprobes. Higher magnification picture is shown on right. Note the presence of nodular C cell hyperplasia in RetM919T/+ mice (right). Scale bars: 100 μm and 20 μm for left and right. (B-D) Whole-mount X-gal staining of E11.5 embryos. (b) The sympathetic trunk (white arrows) was abnormally thick in RetM919T/tlz embryos. Scale bar: 500 μm (c, d) The trigeminal ganglia (white arrowheads), dorsal root ganglia (black arrows) and kidneys (black arrowheads) were comparable between Ret+/tlz and RetM919T/tlz embryos. Scale bars: 500 μm (e) Whole-mount TH immunohistochemistry of E13.5 embryos showed abnormal enlargement of the primary sympathetic chain (white arrows) in RetM919T/tlz mice. Scale bar: 500 μm

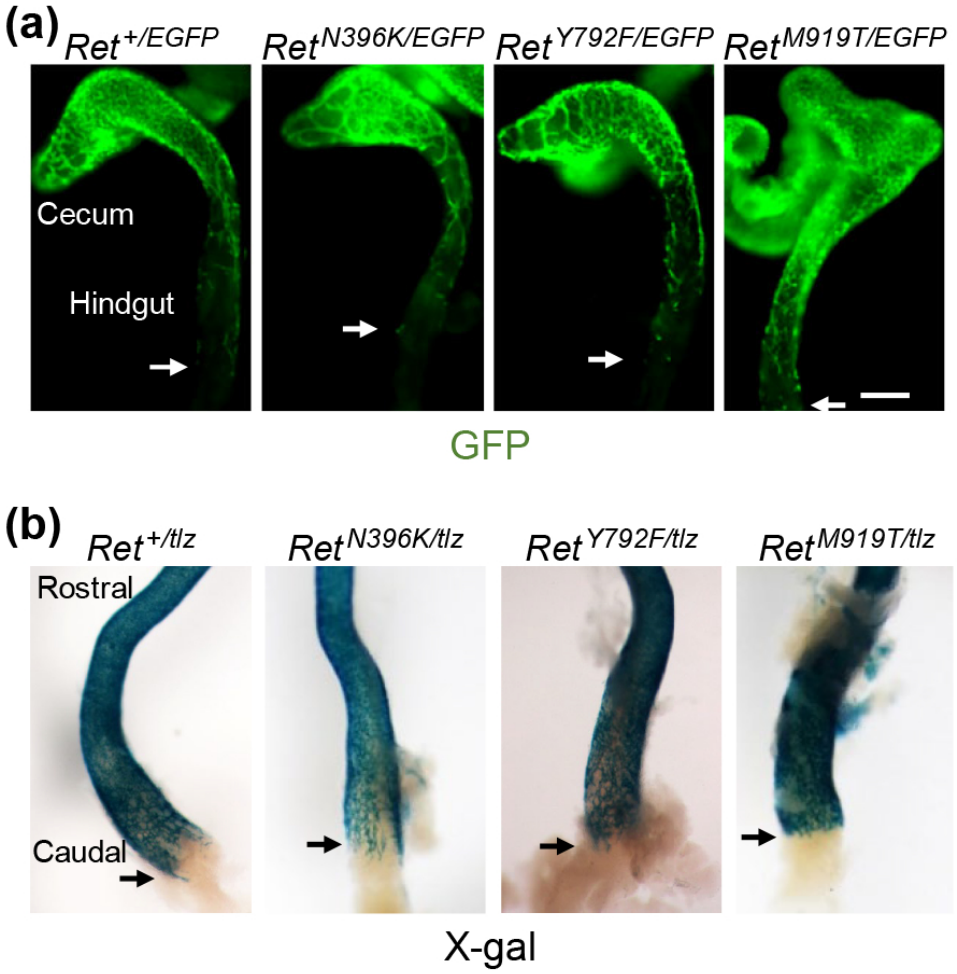

FIGURE 3. Ret missense mutations, N396K, Y792F, and M919T, have no impact on the gut colonization by ENS precursors.
(a) Whole-mount EGFP staining of embryonic gut (E12.5). Arrows indicate the location of most advanced ENS precursors. No difference was observed in Ret+/EGFP, RetN396K/EGFP, RetY792F/EGFP and RetM919T/EGFP embryos. Scale bar: 250 μm. (b) Whole-mount X-gal staining of the distal colon at E15.5 in Ret+/tlz, RetN396K/tlz, RetY792F/tlz and RetM919T/tlz. Colonization pattern by ENS precursors were comparable between all genotypes. Scale bar: 250 μm.

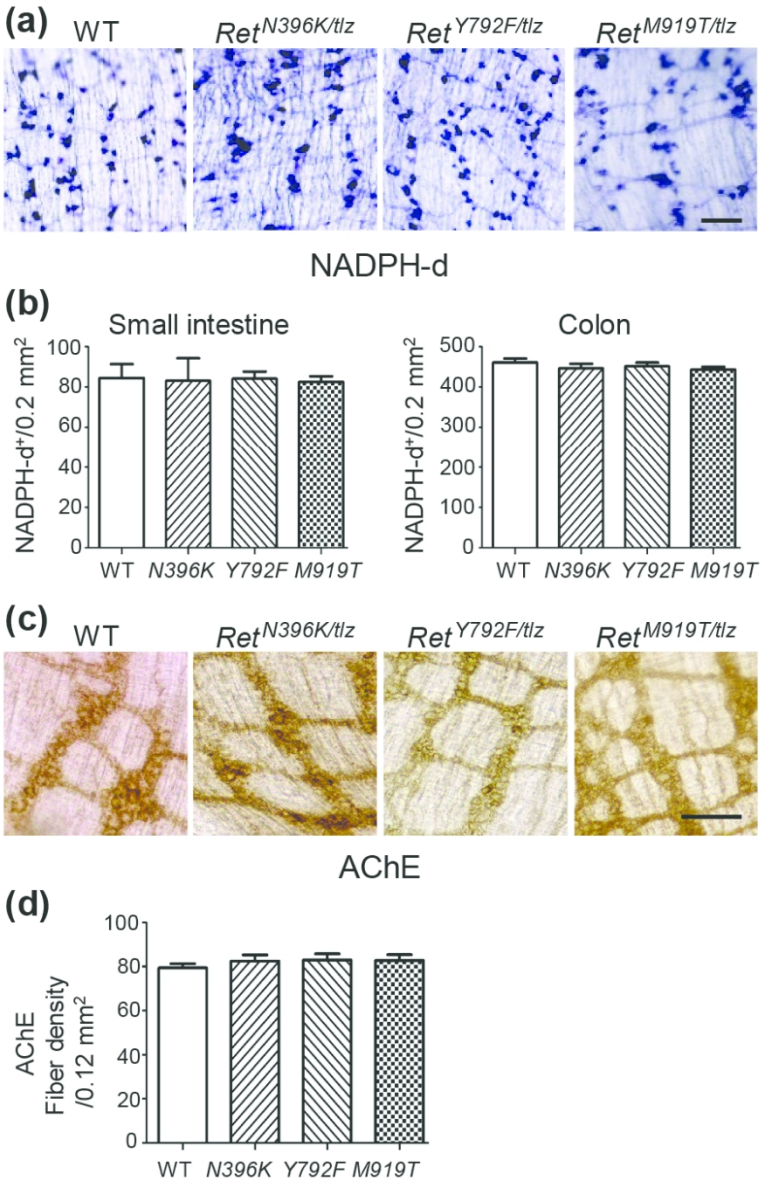

FIGURE 4. Quantitative analysis of enteric neurons in mice carrying Ret missense mutations
(a) Representative images of NADPH-d staining of the small intestine, showing comparable staining patterns in WT, RetN396K/tlz, RetY792F/tlz and RetM919T/tlz mice (P8). Scale bar: 100 μm. (b) Bar graphs showing the numbers of neurons visualized by NADPH-d-staining in the small intestine (left) and colon (right). Error bars: SEM. (c) The structure of the ENS (small intestine, P8) visualized by AChE staining. Scale bar: 100 μm. (d) Bar graph showing the density of AChE-positive fibers in the myenteric plexus of the small intestine. Error bars: SEM.